PNAS RESEARCH ARTICLE | PHYSICS

Hund's flat band in a frustrated spinel oxide

Dongjin Oh[a,1], Alexander Hampel[b], Joshua P. Wakefield[a], Peter C. Moen[c,d], Steef Smit[c,d], Xiangyu Luo[a], Marta Zonno[e], Sergey Gorovikov[e], Mats Leandersson[f], Craig Polley[f], Asish K. Kundu[g], Anil Rajapitamahuni[g], Elio Vescovo[g], Chris Jozwiak[h], Aaron Bostwick[h], Eli Rotenberg[h], Masahiko Isobe[i], Manish Verma[j], Matteo Crispino[j], Martin Grundner[k,l], Fabian B. Kugler[b,m], Olivier Parcollet[b,n], Ulrich Schollwöck[k,l], Hidenori Takagi[i,o,p], Andrea Damascelli[c,d], Giorgio Sangiovanni[j], Joseph G. Checkelsky[a], Antoine Georges[b,q,r,s,1], and Riccardo Comin[a,1]

Affiliations are included on p. 8.

Contributed by Antoine Georges; received July 11, 2025; accepted October 3, 2025; reviewed by Donglai Feng and Jan Kunes

Electronic flat bands associated with quenched kinetic energy and heavy electron mass have attracted great interest for promoting strong electronic correlations and emergent phenomena such as high-temperature charge fractionalization and superconductivity. Intense experimental and theoretical research has been devoted to establishing the rich nontrivial metallic and heavy fermion phases intertwined with such localized electronic states. Here, we investigate the transition metal oxide spinel LiV_2O_4, an enigmatic heavy fermion compound lacking localized *f* orbital states. We use angle-resolved photoemission spectroscopy and dynamical mean-field theory to reveal a kind of correlation-induced flat band with suppressed interatomic electron hopping arising from intra-atomic Hund's coupling. The appearance of heavy quasiparticles is ascribed to a proximate orbital-selective Mott state characterized by fluctuating local moments as evidenced by complementary magnetotransport measurements. The spectroscopic fingerprints of long-lived quasiparticles and their disappearance with increasing temperature further support the emergence of a high-temperature "bad" metal state observed in transport data. This work resolves a long-standing puzzle on the origin of heavy fermion behavior and unconventional transport in LiV_2O_4. Simultaneously, it opens a path to achieving flat bands through electronic interactions in *d*-orbital systems with geometrical frustration, potentially enabling the realization of exotic phases of matter such as the fractionalized Fermi liquids.

flat band | heavy fermion transition metal compound | frustrated lattice | Hund's coupling

Significance

The *d*-orbital heavy fermion behavior observed in the transition metal oxide spinel LiV_2O_4 has remained a subject of controversy and inconclusive interpretation. In this study, we systematically investigated the three-dimensional electronic structure of LiV_2O_4 using angle-resolved photoemission spectroscopy combined with dynamical mean-field theory simulations. Our findings reveal the emergence of a correlation-induced flat band at the Fermi level and underscore the pivotal role of Hund's coupling in driving the heavy fermion behavior. This work provides crucial insights into the origin of heavy fermion physics in LiV_2O_4 and establishes design principles for engineering flat electronic bands via strong local interactions in multiorbital systems.

The motion of electrons in many solids can be largely understood in terms of their kinetic energy. For example, noninteracting electrons can easily hop between atomic sites (a process characterized by a hopping amplitude t), allowing them to delocalize across the solid. The greater the hopping amplitude, the greater the kinetic energy and resulting bandwidth. Such itinerant electrons are described by the free electron model with quadratic dependence of the single-particle energy E on crystal momentum k for small k (Fig. 1*A*) (1). In contrast, the kinetic energy of the noninteracting electrons is quenched in a geometrically frustrated lattice. For example, in the case of the kagome lattice, the flat band originates from quantum destructive interference between atomic sites with opposite phases (Fig. 1*B*). As a result, electrons are "trapped" within the hexagon and form localized electron packets (2–4). This mechanism of geometrical hopping frustration gives rise to an electronic flat band and enhances the electron effective mass.

In addition to lattice-driven interference, electronic motion can also be frustrated by strong interaction effects. In *f*-orbital systems, itinerant electrons (*i*-electrons) strongly interact with the localized, heavy *f*-electron through antiferromagnetic exchange coupling, the so-called Kondo interaction (6), as shown in Fig. 1*C*. The hybridization between these light and heavy electrons leads to the formation of heavy quasiparticle states (Fig. 1*C*). The correlation-induced electron mass enhancement can in principle occur even in the absence of *f*-orbital electronic states. Coulomb repulsion (U) and Hund's coupling (J_H), the latter being a pure interorbital effect, significantly renormalize the bandwidth (W) and electron mass to reduce the effective kinetic energy via the formation of dressed electronic quasiparticles (Fig. 1*D*) (7–9). These forms of correlation-induced electron localization and mass enhancement have been extensively studied in strongly correlated electron systems, such as cuprate (10, 11), iron-based (12), nickelate (13–15), and ruthenate superconductors (16, 17). Here, we investigate the possibility of realizing flat band states through interaction effects.

The realization of correlation-induced flat bands is of significant interest in condensed matter physics. Flat band can host strong correlation effects associated with large effective masses and an enhanced quasiparticle density of states. When an electronic flat band lies at

Author contributions: D.O., A.H., J.P.W., G.S., J.G.C., A.G., and R.C. designed research; D.O., A.H., J.P.W., P.C.M., S.S., X.L., M.Z., S.G., M.L., C.P., A.K.K., A.R., E.V., C.J., A.B., E.R., M.I., M.V., M.C., M.G., F.B.K., O.P., U.S., H.T., A.D., G.S., J.G.C., A.G., and R.C. performed research; D.O., A.H., J.P.W., M.G., F.B.K., O.P., U.S., G.S., A.G., and R.C. analyzed data; J.P.W., M.I., H.T., and J.G.C. synthesized and characterized samples; and D.O., A.H., J.P.W., P.C.M., S.S., X.L., M.Z., S.G., M.L., C.P., A.K.K., A.R., E.V., C.J., A.B., E.R., M.I., M.V., M.C., M.G., F.B.K., O.P., U.S., H.T., A.D., G.S., J.G.C., A.G., and R.C. wrote the paper.

Reviewers: D.F., University of Science and Technology of China; and J.K., Masaryk University.

The authors declare no competing interest.

[1]To whom correspondence may be addressed. Email: djoh@mit.edu, ageorges@flatironinstitute.org, or rcomin@mit.edu.

This article contains supporting information online at https://www.pnas.org/lookup/suppl/doi:10.1073/pnas.2518213122/-/DCSupplemental.

Published November 6, 2025.

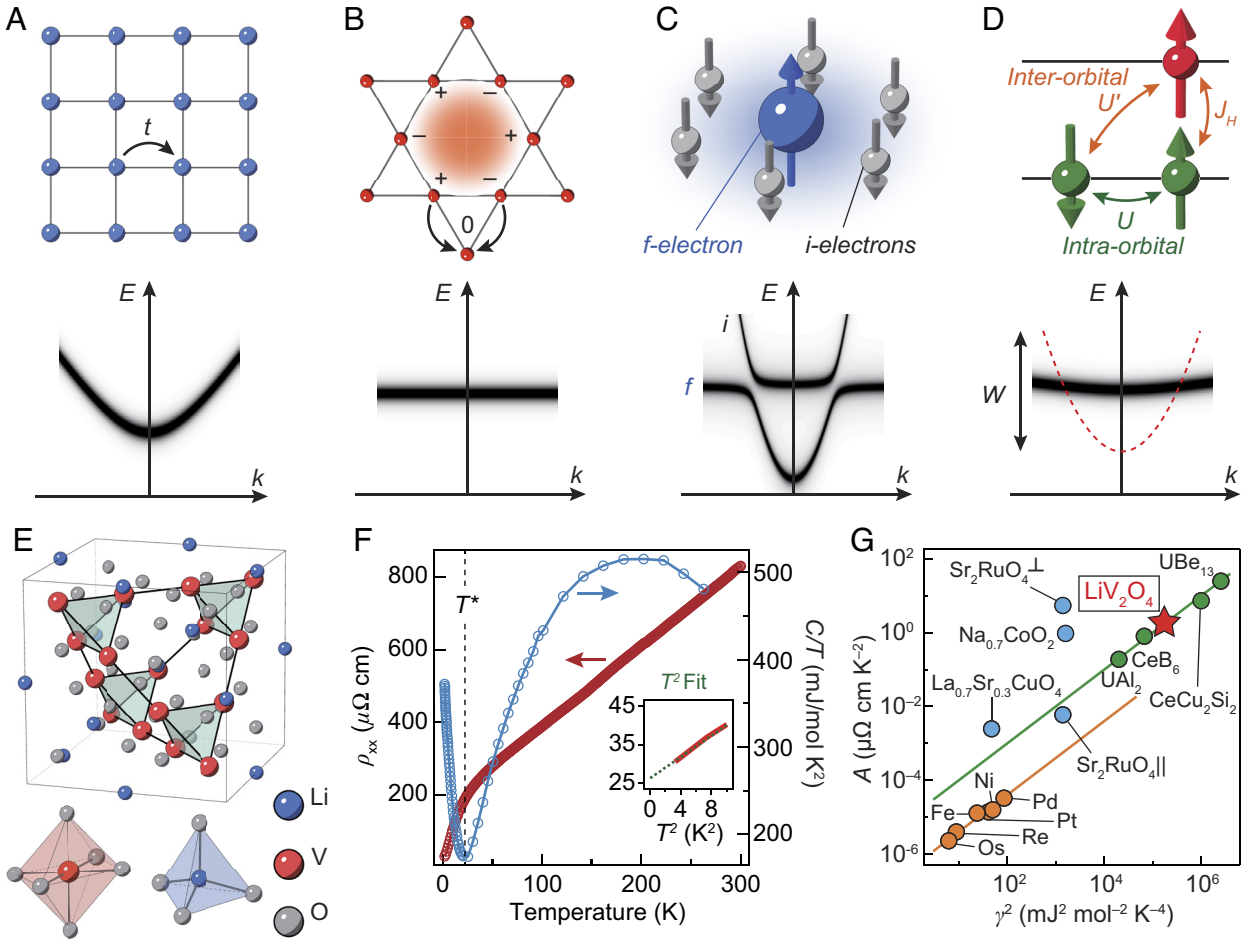

Fig. 1. Heavy fermion behavior of LiV_2O_4. (*A–D*) Representative electronic band structures of the free electron model (*A*); flat band induced by geometrical frustration in the kagome lattice (*B*); hybridization between localized *f*-electron and itinerant electrons (*i*-electrons) (*C*); and bandwidth renormalization induced by strong electron correlation via intraorbital Coulomb (*U*), interorbital Coulomb (*U'*), and Hund's coupling (J_H) (*D*). The red dashed curve corresponds to the bare band dispersion without electron correlations. (*E*) Crystal structure of LiV_2O_4 composed of VO_6 octahedra and LiO_4 tetrahedra. The V atoms form a frustrated pyrochlore network. (*F*) Heavy Fermi liquid behavior of LiV_2O_4. The temperature-dependent electrical resistivity (red circles) shows a coherent-incoherent crossover while the electronic specific heat *C*/*T* (blue circles) shows a large Sommerfeld coefficient $\gamma \approx 420$ mJ/mol K^2. The *Inset* shows ρ_{xx} versus T^2 plot (red) and T^2 fitting result (green). (*G*) The Kadowaki–Wood ratio of various materials, defined as the ratio of the coefficient of the T^2 term in electrical resistivity and γ^2. LiV_2O_4 lies close to *f*-electron heavy fermion systems (green circles and line). Orange and blue circles represent the Kadowaki–Wood ratio of transition metals and oxide compounds, respectively. The value of the Kadowaki–Wood ratio was adapted from ref. 5.

the Fermi level, it makes the electronic ground state unstable toward ordered phases such as unconventional superconductivity (18), quantum magnetism, integer (19) and fractional quantum anomalous Hall effect (20), and anomalous Landau levels (21). Due to these unique characteristics of electronic flat bands, significant efforts are directed toward realizing flat bands not only in crystalline solids (3, 4, 22–26) but also in photonic lattices (27, 28), phononic (29) and magnonic crystals (30), and metal-organic frameworks (31). Therefore, exploring new ways to construct electronic flat bands and broadening the materials platform that can host such states is a timely challenge and opportunity for quantum material research.

Lithium vanadate (LiV_2O_4) is an ideal candidate to explore novel mechanisms of flat band formation. This transition metal oxide compound crystallizes in the spinel structure and its low-energy electronic structure is governed by *d*-orbital electrons. LiV_2O_4 is the material that displays heavy Fermi liquid behavior with heaviest mass despite not containing *f*-electron states (32–34). Indeed, this material possesses all the ingredients for supporting an electronic flat band. The V ions of LiV_2O_4 comprise a frustrated pyrochlore network (Fig. 1*E*) that can host frustration-induced compact localized states and a corresponding three-dimensional flat band (2, 24). Moreover, it has been argued that magnetic frustration within the pyrochlore lattice can also be an essential factor in emerging heavy fermion behavior (33, 35–40). Within the theoretical framework, strong electron correlation effects mediated by the Coulomb, Hund, and Kondo interactions have been actively discussed (36–38, 40–44). The electronic specific heat of LiV_2O_4 with large Sommerfeld coefficient $\gamma \sim 420$ mJ/mol K^2 (blue circles in Fig. 1*F*) is the first important fingerprint of heavy electrons (32, 33) (uncorrelated metals typically have $\gamma < 20$ mJ/mol K^2, and heavy fermion metals with *f*-electrons have $\gamma \approx 100 \sim 1{,}000$ mJ/mol K^2). Remarkably, the value of the Kadowaki–Wood ratio (the ratio of the coefficient of the T^2 term in electrical resistivity and γ^2) is in line with that of *f*-electron heavy fermion systems (Fig. 1*G*) (5). In addition, temperature-dependent electrical resistivity data indicate incoherent "bad" metallic behavior at high temperatures, with a crossover to a coherent metallic state below $T^* \sim 25$ K (red curve in Fig. 1*F*) (33). A Fermi liquid state eventually materializes below 2 K (45). These thermodynamic and electrical properties imply the presence of heavy quasiparticles at low temperatures. However, the precise microscopic mechanisms responsible for generating such heavy bands have remained elusive.

Here, we present experimental and theoretical findings that provide conclusive insight into the origin of heavy fermion

behavior in LiV_2O_4. We investigate the electronic band structure of LiV_2O_4 in three-dimensional (3D) momentum space using temperature- and photon energy-dependent angle-resolved photoemission spectroscopy (ARPES) experiments. ARPES data provide direct evidence for a coherent electronic flat band at the Fermi level. We further find that this coherent heavy quasiparticle state partly survives in the bad metallic regime up to 140 K, becoming fully incoherent above this temperature. Our experimental observation of the correlated flat band is supported by first-principles calculations based on the dynamical mean-field theory (DMFT) framework, which identify orbital differentiation driven by Hund's coupling J_H as the crucial mechanism that drives the formation of the flat band and associated heavy fermion behavior in LiV_2O_4. The orbital-specific correlated flat band results in a highly localized electron state with fluctuating local moment as evidenced by negative MR and in agreement with other experimental results on LiV_2O_4 (33, 35). Our study not only reveals the origin of heavy fermion behavior in this specific compound but may provide a generalizable strategy to produce heavy electronic bands in *d*-electron systems. Furthermore, the direct observation of heavy quasiparticles in a frustrated lattice may serve as a foundation for the experimental realization of novel phases of matter such as a fractionalized Fermi liquid (46, 47).

Results

ARPES spectra of LiV_2O_4 are shown in Fig. 2. A clear Fermi surface near the Γ point (k_z = 0 Å^{-1}) was observed with several Fermi pockets consistent with the metallic behavior (Fig. 2*A*). To map out the three-dimensional electronic band structure along k_x, k_y, and k_z crystal momenta across the 3D Brillouin zone (Fig. 2*B*), we performed photon energy-dependent ARPES measurements. Fig. 2 *C* and *D* shows the energy–momentum dispersion obtained at 6 K and 165 K, respectively, along the L-Γ-L *k*-path aligned to the k_z axis in the experimental coordinate system (Fig. 2*B*). Both the low- and high-temperature spectra exhibit a broad electron-like conduction band between −0.4 ~ 0 eV binding energy near the Γ point ($h\nu$ = 95 eV). The strong modulation of this feature with respect to the photon energy (k_z momentum) is suggestive of the three-dimensional nature of the electronic band structure of LiV_2O_4. Interestingly, the low-temperature ARPES spectrum exhibits an additional sharp peak at the Fermi level over

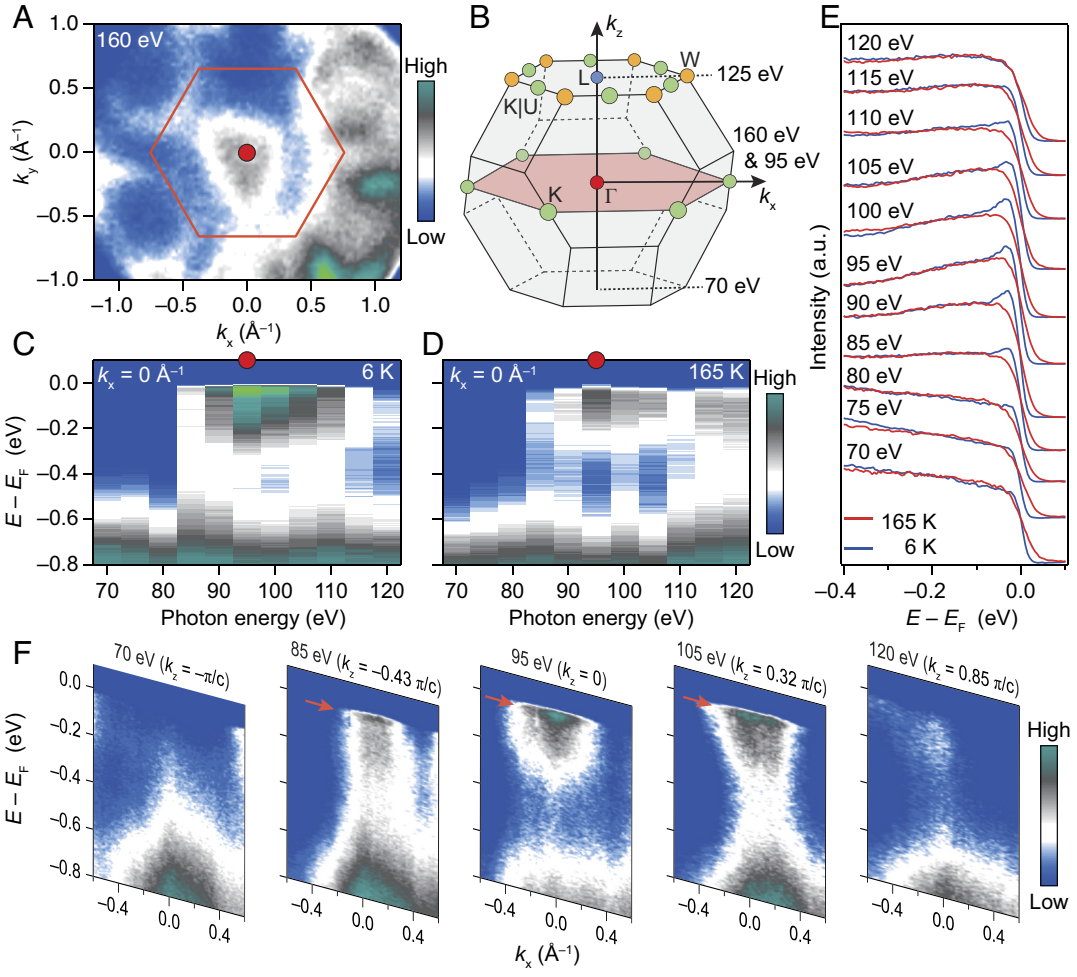

Fig. 2. Observation of a flat band. (*A*) Fermi surface of LiV_2O_4 near the k_z = 0 Å^{-1} plane. The red hexagon and circle represent the first Brillouin zone and Γ point, respectively. (*B*) Three-dimensional bulk Brillouin zone. Red, green, blue, and yellow circles correspond to the high symmetry Γ, K|U, L, and W points, respectively. In the experimental geometry, the k_x and k_z momenta are aligned to the K-Γ-K and L-Γ-L directions, respectively. 95 eV and 160 eV photon energies probe the k_z = 0 Å^{-1} momentum plane. On the other hand, 70 eV and 125 eV photon energies measure the k_z = π/c plane. (*C* and *D*) Low (*C*) and high (*D*) temperature energy–momentum dispersion across the L-Γ-L *k*-path aligned to the k_z momentum. (*E*) Comparison between low and high temperature EDCs measured at the different photon energies. Red and blue EDCs were measured at 6 K and 165 K, respectively. Each EDC is integrated within k_x = ±0.1 Å^{-1}. (*F*) Photon energy-dependent energy–momentum dispersion along k_x, measured at 6 K. Red arrows indicate the observed flat band.

a wide k-path from $h\nu$ = 85 eV (k_z = −0.43 π/c) to 110 eV (k_z = 0.5 π/c) (46% of the Brillouin zone size, along L-Γ-L). The energy distribution curves (EDCs) in Fig. 2*E* clearly display the emergence of a sharp quasiparticle peak at the Fermi level at low temperature, providing direct signature of an electronic flat band along the L-Γ-L high symmetry line. Furthermore, ARPES spectra aligned to the in-plane momentum k_x confirm the presence of an extended flat band. Fig. 2*F* shows the measured in-plane ARPES spectra at various out-of-plane k_z momenta, with the flat spectral weight between k_z = −0.43 and 0.32 π/c marked by red arrows. These systematic ARPES measurements directly demonstrate the formation of a low-energy flat band in LiV_2O_4, consistent with the reported heavy fermion behavior.

We further carried out temperature-dependent ARPES measurements to trace the evolution of the flat band. Fig. 3 *A*–*F* shows the in-plane energy–momentum dispersion near the Γ point measured from 6 K to 160 K. At 6 K, a sharp spectral weight of the flat band is discerned within $k_x \approx \pm 0.4$ Å^{-1} (50% of the high symmetry K-Γ-K k-path), on top of a broad hump. The presence of sharp spectral features at the Fermi level indicates the formation of coherent quasiparticles, as per Landau's Fermi liquid formalism. Therefore, the observed sharp flat band in the low-temperature ARPES data can be identified with heavy coherent quasiparticles in LiV_2O_4. The coherent spectral weight is significantly renormalized with temperature, as shown in the EDCs. The sharp coherent peak at the Fermi level gradually disappears with increasing temperature and becomes almost indiscernible around 160 K (Fig. 3*G*). The spectral weight of the flat band, defined as the intensity in the gray area of Fig. 3*G* subtracted by that of 160 K, shows a temperature-dependent loss of coherence with increasing temperature (Fig. 3*H*). Furthermore, the width of the flat band along k_x (indicated by the orange arrow in Fig. 3*A*) also becomes gradually narrower upon increasing temperature as shown in Fig. 3 *H* and *J* (*SI Appendix,* Fig. S2). We note that the coherent heavy quasiparticle band is robust even in the bad metallic regime ($T > T^* \sim 25$ K), which is counterintuitive to the notion that a coherent quasiparticle state cannot exist within a bad metallic regime, similar to the behavior of the resilient quasiparticle (48). Our ARPES results suggest that understanding the flat band formation mechanism requires consideration of effects beyond the single-particle picture, as achieved by our DMFT analysis.

To elucidate the microscopic origin of the correlated flat band in LiV_2O_4, we calculate the momentum-dependent spectral function via a combination of density functional theory plus dynamical mean-field theory (DFT+DMFT), which is a reliable methodology to account for many-body electron correlation effects (49). The realistic Coulomb interaction obtained from first-principle calculations and the DMFT impurity problem is solved by the numerically exact QMC solver. Fig. 4*A* shows the orbital-integrated DMFT spectral function at T = 11.6 K, which displays a sharp, flat, and extended quasiparticle band very close to the Fermi level (E = −1.75 meV at Γ). In LiV_2O_4 (as well as other oxide spinels),

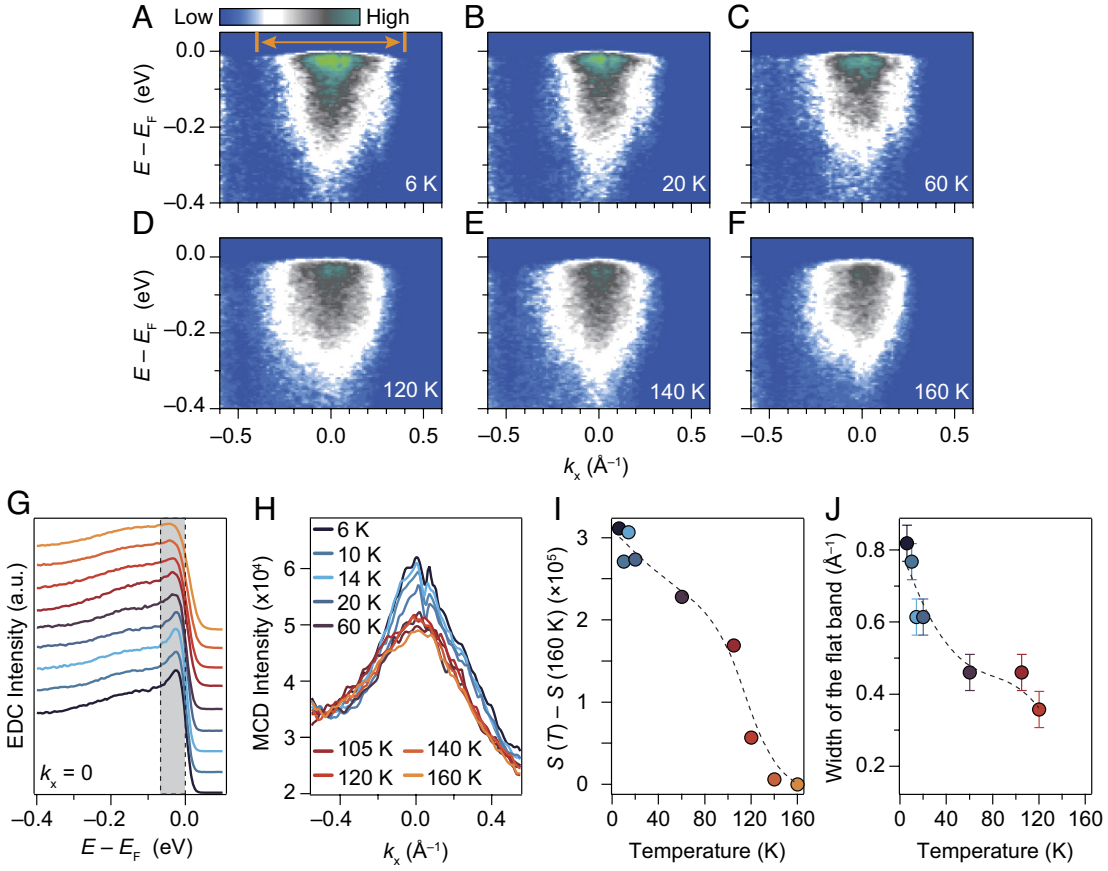

Fig. 3. Temperature evolution of the flat band. (*A*–*F*), Temperature-dependent ARPES maps across the Γ point (k_y and k_z = 0 Å^{-1}). (*G* and *H*) Temperature-dependent EDCs extracted from k_x = 0 Å^{-1} (*G*) and momentum distribution curves (MDCs) near the Fermi level. Each EDC is integrated within k_x = ±0.09 Å^{-1}. The EDCs were normalized with the integrated intensities from −0.4 eV to −0.3 eV and shifted vertically. (*I*) Temperature dependence of the flat band spectral weight, defined as the integrated intensity in the gray area of (*G*) subtracted by the intensity at 160 K. (*J*) Temperature dependence of the width of the flat band, defined as the momentum range of the region where the quasiparticle peak is identified as indicated by the orange arrow in (*A*) (*SI Appendix,* Fig. S2). Error bars reflect the integrated momentum window.

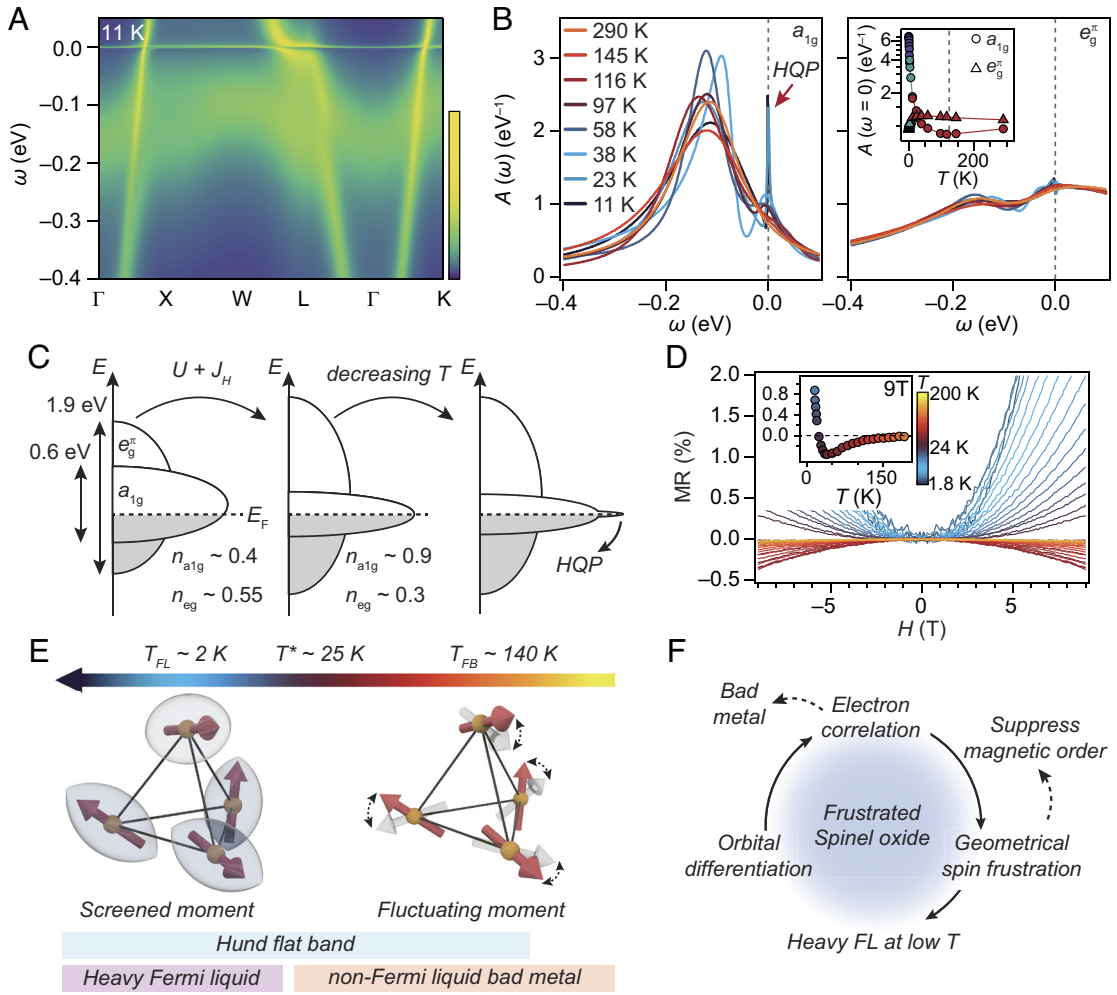

Fig. 4. DMFT spectral functions and flat band formation mechanism. (*A*) Momentum-dependent spectral function of LiV_2O_4 across the high symmetry *k*-points. (*B*) Momentum integrated spectral function of a_{1g} (*Left*) and e_g^π (*Right*) orbitals at various temperatures. The *Right* panel *Inset* represents the temperature-dependent intensity of spectral functions at the Fermi level. Circles and triangles indicate the intensity of a_{1g} and e_g^π orbitals, respectively. Purple, green, and red points are calculated by NRG, TN, and QMC methods, respectively. (*C*) Schematic energy diagram for the band structure renormalization. (*D*) MR, $[\rho_{xx}(H) - \rho_{xx}(0)]/\rho_{xx}(0)$, of LiV_2O_4 at various temperatures. The *Inset* shows the temperature-dependent MR at 9 T for temperatures down to 16 K. (*E*) Schematic temperature evolution of LiV_2O_4. Yellow spheres and red arrows represent V ions and a_{1g} local moments. T_{FL} and T_{FB} are abbreviations for Fermi liquid and flat band onset temperature, respectively. (*F*) Possible flat band formation mechanism in the frustrated spinel oxide.

V ions are surrounded by oxygens, forming VO_6 octahedra with trigonal distortion (*SI Appendix*, Fig. S3). This trigonal distortion splits the t_{2g} manifolds into an a_{1g} singlet and an e_g^π doublet. The orbital projected spectral function calculation identifies the narrow flat band mainly composed of the a_{1g} orbital while the e_g^π orbital exhibits dispersive bands. The temperature-dependent orbital projected local spectral functions shown in Fig. 4*B* demonstrate the emergence of a quasiparticle peak in the a_{1g} orbital manifold below 140 K, consistent with ARPES results (*Inset* of Fig. 4*B*). Below 38 K, the a_{1g} spectral function shows a rapidly growing heavy quasiparticle peak at the Fermi level while the e_g^π orbital bands undergo minor renormalization (*SI Appendix*, Fig. S4). We note that the correlated a_{1g} flat band does not arise from the compact localized states of the frustrated pyrochlore lattice. At the DFT level, an electronic flat band derived from the compact localized state of e_g^π orbital character is well above the Fermi level and is linked to the typical band structure of the pyrochlore lattice (50). Also in DMFT, the flat band of the e_g^π orbital remains 0.6 eV above the Fermi level (*SI Appendix*, Fig. S4). Therefore, the a_{1g} flat band is a purely correlated electronic flat band, in contrast to that recently reported flat band in chalcogenide spinel CuV_2S_4 driven by geometrical hopping frustration (51).

It is important to note that while our DMFT spectral function reveals a correlated flat band spanning the entire momentum space, our ARPES spectra capture only a part of it. This might be due to the finite dispersion of the flat band. According to our DMFT calculation shown in *SI Appendix*, Fig. S5 (see also *SI Appendix*, *Text 1*), the flat band exhibits weak electron-like dispersion near the Γ point within a narrow energy range near the Fermi level (*SI Appendix*, Fig. S7 and *Text 2*). Due to this dispersion, the flat band is positioned below the Fermi level within the momentum range of $k_x = \pm 0.5$ Å^{-1}. Indeed, our ARPES spectra obtained at base temperature clearly captured the flat band spectral weight within the range of $k_x = -0.41 \pm 0.05$ Å^{-1} to $k_x = +0.41 \pm 0.05$ Å^{-1}. Similarly, the k_z dispersion of the flat band also reveals electron-like dispersion (*SI Appendix*, Fig. S7 and *Text 2*). Thus, the flat band lies below the Fermi level at the Γ point and crosses the Fermi level near $k_z = \pm 0.71$ π/c. Our ARPES spectral weight confirms the flat band dispersion within the momentum range of $k_z = -0.43$ π/c to $k_x = 0.5$ π/c. While the ARPES data capture the flat band spectral weight in the anticipated momentum ranges,

minor mismatches are observed. These discrepancies are likely due to the photoemission matrix element effects. Indeed, a laser-based angle-integrated photoemission measurement with 7 eV photon energy (which probes $k_z = 0.76\,\pi/c$) successfully detected the quasiparticle peak above the Fermi level (52). This emphasizes the critical role of matrix element effects. While our synchrotron-based ARPES, using photon energies ranging from 70 to 190 eV, was unable to detect the quasiparticle peak near the L point, it has been clearly resolved with a 7 eV laser. This suggests that the absence of the quasiparticle peak in our ARPES data away from the Γ point arises from a combination of 3D dispersion and matrix element effects.

It is also worth noting that spectral width of the observed ARPES spectra is significantly broader than that predicted by DMFT calculations. In principle, the intrinsic peak width of the ARPES spectral weight is governed by the quasiparticle self-energy. However, extrinsic factors—such as experimental resolution, photoelectron scattering during the photoemission process, and k_z broadening—also contribute to the observed broadening, whereas these factors are absent in our DMFT simulations. We find that the full width at half maximum of the quasiparticle peak is approximately 35 meV, which is comparable to the experimental resolution of the synchrotron-based ARPES setup. This suggests that the experimental resolution is one of the contributing factors to the discrepancies between ARPES and DMFT. Indeed, when we incorporate the effects of experimental resolution into the DMFT spectra, we observed a modest improvement in the agreement (*SI Appendix,* Fig. S6). Therefore, high-resolution ARPES experiments with enhanced energy resolution could further improve the consistency between experimental data and theoretical calculations.

Discussion

The DMFT results strongly indicate that orbital-dependent electron correlations are the most important ingredient in the formation of a correlated flat band in LiV_2O_4 (50, 53). This orbital differentiation is a result of the combination of the unique crystalline symmetry of the oxide spinels and Hund's coupling J_H. In the noninteracting limit without considering electron correlation (U and J_H), the a_{1g} orbital has a relatively narrow bandwidth (~0.7 eV) and large peak near the Fermi level while the e_g^π levels have a broad bandwidth (~1.9 eV) as shown in Fig. 4*C*. In this limit, the a_{1g} and e_g^π orbitals have 0.4 and 0.55 electrons per V ion, respectively (50). When we consider U (3.94 eV), the electron filling of the a_{1g} orbital increases up to 0.7 electrons per V ion in contrast to the e_g^π which is reduced to 0.4 electrons. The inclusion of J_H (0.56 eV) further promotes the orbital differentiation by pushing more electrons into the a_{1g} band, with an electron count of 0.9 electrons per V ion. Therefore, the effect of J_H is to make the a_{1g} (e_g^π) states more localized (delocalized) while lowering their kinetic energy. As a result, Hund's coupling brings LiV_2O_4 in proximity of an orbital selective Mott phase (OSMP) (8, 54), with a hole doping of ~10%. However, due to the interorbital hybridization between a_{1g} and e_g^π bands, LiV_2O_4 does not enter the OSMP but rather exhibits the strongly correlated metallic state with heavy quasiparticles upon cooling (55, 56).

This phenomenon is reminiscent of the general trend in Hund's metals where interorbital coupling is the dominant factor behind electron correlations (8, 9, 12, 57). The correlated metallic behavior of the a_{1g} electrons is closely related to the Hund's metal physics accompanied by Hund's coupling induced fluctuating local moment and paramagnetic (no long-range magnetic order) incoherent metallic behavior (58). This fluctuating local moment of LiV_2O_4 is corroborated by the paramagnetic Curie–Weiss behavior and the nonsaturating incoherent transport at high temperatures (32, 33). We note that, in the spin fluctuation regime, an external magnetic field makes the transport more coherent by polarizing the disordered local moments and reducing scattering from spin fluctuations (59). As a result, negative magnetoresistance (MR) is expected in the incoherent metal region. Magnetotransport measurements on LiV_2O_4 (Fig. 4*D*) confirm this scenario through the clear negative MR in the incoherent transport regime. The fluctuating local moment is supported by other experimental data, namely the presence of spin fluctuations in the incoherent metallic regime of the LiV_2O_4 (35, 40). Notably, similar negative MR driven by spin fluctuation has also been reported in Mn-based kagome metal where J_H plays a significant role (60).

Fig. 4*E* summarizes the temperature evolution of the macroscopic phenomena occurring in LiV_2O_4. First, the heavy a_{1g} orbital, which is highly localized by Hund's coupling J_H, forms a fluctuating local moment at high temperature and strongly suppresses the coherence stabilizing the incoherent bad metallic behavior (8, 50, 61). As temperature decreases, a correlated a_{1g} flat band associated with the heavy quasiparticle state occurs. When the local moment is completely screened at low temperatures, LiV_2O_4 displays heavy Fermi liquid behavior in electrical resistivity and Pauli behavior in magnetic susceptibility (32).

Through the combination of ARPES, magnetotransport, and DMFT, we conclusively demonstrate the presence of a correlation-induced flat band as the key ingredient in the heavy fermion behavior in LiV_2O_4. These observations highlight spinel oxides as promising material candidates to explore a pathway toward correlated flat bands (Fig. 4*F*). As discussed above, the trigonal splitting of the octahedral crystal field in the spinel structure initiates the orbital differentiation. Then, J_H boosts the crystal field splitting and orbital-dependent electron correlation (8). In this respect, oxide spinels have an advantage over chalcogenide spinels due to their strong ligand field originating from the large electronegativity of oxygen. Therefore, noticeable orbital differentiation in a_{1g} and e_g^π orbitals can arise in oxide spinels in conjunction with J_H. When two orbitals satisfy the appropriate electron filling, correlated electronic states with heavy effective mass enhanced by a spin blocking mechanism and fluctuating local moment can be stabilized (50, 58). In this circumstance, bad-metallic behavior may appear as a by-product. This orbital-dependent correlation in LiV_2O_4, promoted by J_H, stands in stark contrast to the electronic correlation in the chalcogen spinel compound CuV_2S_4 where the crystal field splitting of t_{2g} manifold is absent and the distinct electronic correlation effects between these two compounds may explain their contrasting material properties, such as the absence of heavy fermion behavior in CuV_2S_4 (51).

However, the orbital-dependent correlation effect alone is not sufficient to make *d*-electrons sufficiently heavy. Previous studies have reported experimental evidence of heavy fermion behavior in *d*-orbital systems such as $Ca_{1.5}Sr_{0.5}RuO_4$ (62), YMn_2Zn_{20} (63), $(Y_{0.97}Sc_{0.03})Mn_2$ (64), Fe_3GeTe_2 (65), FeTe (66), $Cs(Fe_{0.97}Cr_{0.03})_2As_2$ (56). Interestingly, a trend can be identified whereby a reasonably large Sommerfeld coefficient appears only in materials without long-range magnetic order: FeTe and Fe_3GeTe_2, which have antiferromagnetism and ferromagnetism, respectively, exhibit the smallest Sommerfeld coefficient among the above series. This tendency implies that long-range magnetic order competes with *d*-orbital heavy fermion behavior, an effect that was systematically studied in

Cr-doped $CsFe_2As_2$ (56). In that sense, the suppression of long-range magnetic order and the effective superexchange via geometrical spin frustration in the pyrochlore sublattice (distinct from the fluctuating local moments induced by Hund's coupling) of oxide spinels may be an important factor in fostering *d*-orbital heavy fermion behavior (50). Although most of the AB_2O_4 oxide spinels which have integer valence state in the *B* site have been known as a Mott insulator, the heavy electronic state may be realized via systematic chemical composition engineering by inducing a mixed valence state with $n_V > 1$ as in the case of LiV_2O_4. For example, systematic studies on the strongly correlated metal-to-insulator transition upon chemical substitution from AV_2O_4 (*A* = Mg, Zn) with $n_V = 2$ to Li end ($n_V = 1.5$) (67, 68) or electrochemical Li (de)intercalation to the LiV_2O_4 ($1 \leq n_V \leq 2$) (69, 70) may enable further control and engineering of correlation-induced flat bands.

Recent discussions have highlighted the intimate connection between the flat band and Hund's coupling J_H in the high-temperature superconductor $La_3Ni_2O_7$ (15). DMFT calculations reveal that J_H promotes the formation of flat bands through orbital-dependent correlations. However, this DMFT on nickelate superconductor also predicts strong antiferromagnetic coupling of the local moment, which contrasts with LiV_2O_4, where weak spin correlations arise due to geometrical frustration. Similarly, another DMFT study on $CsCr_3Sb_5$ and CrB_2 also underscores the crucial role of J_H in the heavy fermion behavior associated with d-orbital electrons (71). While these theoretical works support the applicability of our proposed approach for implementing a heavy quasiparticle electronic state at the Fermi level in other systems, this theoretical proposal remains experimentally unverified in these materials (14, 72).

Furthermore, there has been active discussion about how to screen the high-spin electrons in Hund's metals and enter the Fermi liquid state within the DMFT framework (57, 58, 73–76). The frustrated oxide spinel compounds could serve as ideal material candidates for experimentally validating these novel theoretical models. Moreover, it was pointed out that exotic heavy Fermi liquid phase with fractionalized excitation favors nonmagnetic frustrated lattice systems (46). Therefore, future research on LiV_2O_4 and other frustrated spinel oxides, aiming to realize a heavy fermion state via local correlation effects, may pave the way to discovering new quantum phases of matter.

Materials and Methods

Single-Crystal Growth and Characterization. Single crystals of LiV_2O_4 were grown following a previous report (77) out of a melt containing 58% by weight LiV_2O_4 powder and 42% by weight Li_3VO_4. The powders were placed in a platinum crucible and heated in a quartz tube under vacuum to 1,050 °C, held at this temperature for 1 d, and then cooled over 5 d to 930 °C after which the furnace was shut off. LiV_2O_4 crystals were separated from the flux by washing with water. LiV_2O_4 powder was grown out of a reaction containing Li_3VO_4, V_2O_3, and V_2O_5 in a 4:9:1 molar ratio. The reactants were pelletized and wrapped in Au foil before being sealed under vacuum in a quartz tube and heated at 700 °C for 2 d. Li_3VO_4 was obtained by a reaction between Li_2CO_3 and V_2O_5 in a 3:1 ratio in air at 800 °C for 20 h. Single crystals used for the magnetotransport measurements as well at ARPES experiments carried out at the National Synchrotron Light Source II (NSLS II) were further annealed at 700 °C in vacuum wrapped in Au foil also containing powder LiV_2O_4 for up to a week. Magnetotransport measurements were taken in a 4 contact geometry with current in the (111) plane and field perpendicular to the (111) plane. To make ohmic contact to the samples, first a pattern of 3 nm Ti followed by 40 nm Au was deposited onto the sample surface which was then contacted with Au wired by silver paint. Data were collected with a standard ac lock-in method at a typical current of 2 mA at fields between –9 T and 9 T. All field-dependent data are symmetrized with respect to field direction. Specific heat data were taken down to 1.8 K in a commercial cryostat using the thermal relaxation method.

Angle-resolved photoemission spectroscopy. ARPES experiments were performed at Beamline7.0.2 (MAESTRO) of the Advanced Light Source (ALS), the QMSC (Quantum Materials Spectroscopy Centre) beamline of the Canadian Light Source (CLS), the Bloch beamline of the MAX IV laboratory, and the ESM beamline of the NSLS II. All ARPES spectra were obtained from the (111) surface with linear horizontal polarization (*p*-polarization). The LiV_2O_4 crystals were cleaved inside ultrahigh-vacuum ARPES chambers (~4×10^{-11} torr). The obtained cleaved surfaces were always aligned to the [111] crystallographic axis. To minimize beam induced damage that occurs when vacuum ultraviolet light irradiates the LiV_2O_4 crystals, the undulator of the synchrotron facility was intentionally detuned to reduce photon flux as needed. The energy and momentum resolutions were approximately 30 meV and 0.01 $Å^{-1}$, respectively. To estimate the value of k_z momentum, an inner potential V_0 of 15 eV was used.

DFT+DMFT. DFT calculations are performed using the Quantum Espresso software package using the ONCVPSP norm-conserving pseudopotentials (78, 79) in conjunction with the Perdew–Burke–Ernzerhof exchange-correlation functional. Structural parameters are fixed to the experimental values reported at 12 K $a_0 = 8.22694(3)$ Å and $x_0 = 0.26109(2)$ (32). We use a wavefunction cut-off of 90 Ry, a density cut-off of 360 Ry, and a mesh of 11 × 11 × 11 *k*-points resulting in an energy error of <1 meV per formula unit. Further, we construct maximally localized Wannier functions using Wannier90 (80) for the low-energy states around the Fermi level with dominantly V *d*-character. This allows us to define a low-energy Hamiltonian $H^{W90}(R)$ in real space, capturing the essential physics of the system realistically. Furthermore, we rotate the Hamiltonian on each V-site into the crystal field basis to diagonalize both the local noninteracting Hamiltonian and the hybridization function. For high accuracy low-temperature calculations, we leverage Wannier interpolation, Fourier transforming $H^{W90}(R)$ to a dense 41 × 41 × 41 *k*-point mesh to avoid any *k*-discretization error. To determine the effective Coulomb interaction for this low energy model we utilize the constrained random phase approximation (81) as implemented in the RESPACK code (82). We limit ourselves here to the static, $\omega = 0$ limit and fit the obtained four-index Coulomb tensor to the symmetrized Kanamori form (including spin-flip and pair-hopping terms) with three independent parameters. The optimal fit yields $U = 3.94$ eV, $U' = 2.83$ eV, and $J = 0.56$ eV. To cover all *T* regimes, we use a combination of impurity solvers to solve the DMFT equations. For calculations mainly at high temperature down to 11.6 K (1/1,000 eV), we use the continuous-time hybridization-expansion quantum Monte Carlo (QMC) solver as implemented in the TRIQS software library (83, 84) and its interface to electronic structure codes TRIQS/DFTTools and TRIQS/SOLID_DMFT (50, 85, 86). High-frequency noise in the impurity self-energy is suppressed by fitting the tail of Σ_{imp} up to fourth order in a window with moderate noise. The first two moments of the tail expansion are measured to high precision directly in TRIQS/CTHYB (87). All QMC calculations include all pair-hopping and spin-flip terms of the interaction. Second, the $T = 0$ TN-based solver from refs. 8889, 90 was extended to $T > 0$ using thermal-state purification (91, 92). The tensor-network (TN) solver is used down to 2.9 K (1/4,000 eV), while keeping as in QMC all terms of the interaction. Third, to access the sub-1 K regime, we use numerical renormalization group (NRG), similarly as in refs. 93 and 94. To make nondegenerate three-orbital NRG calculations tractable, we increase the local symmetry by neglecting the pair-hopping part of the interaction when using this solver (93). To calculate the real frequency spectral functions shown in the main text from QMC data, we analytically continue the impurity self-energy using Padé approximants and calculate the lattice Green function on the real frequency axis. More technical details on the DMFT calculations and for each solver can be found in ref. 50.

Data, Materials, and Software Availability. Experimental and Computational Datasets data have been deposited in Harvard Database (95). The code for DMFT calculations is accessible via https://github.com/TRIQS/solid_dmft (86) and the SYTEN tensor network code is available at www.syten.eu (96). All other data are included in the manuscript and/or *SI Appendix*.

ACKNOWLEDGMENTS. We appreciate fruitful discussions with S. Todadri and Y. Kim. This work was supported, in part, by the Air Force Office of Scientific Research under grant FA9550-22-1-0432 (ARPES, material synthesis and characterization), the Gordon and Betty Moore Foundation Emergent Phenomena in Quantum Systems Initiative (grant no. GBMF9070 to J.G.C.) (instrumentation

development), and the NSF (DMR-2104964) (thermodynamic measurements). This research used resources of the ALS, which is a Department of Energy (DOE) office of Science User Facility under contract no. DE-AC02-05CH11231. This research used resources from the ESM beamline of the NSLS II, a US DOE Office of Science User Facility operated for the DOE Office of Science by Brookhaven National Laboratory under Contract No. DE-SC0012704. We acknowledge MAX IV laboratory for time on Bloch beamline under proposal 20230565. Research conducted at MAX IV, a Swedish national user facility, is supported by the Swedish Research council under contract 2018-07152, the Swedish Governmental Agency for Innovation Systems under contract 2018-04969, and Formas under contract 2019-02496. This research was undertaken thanks in part to funding from the Max Planck–University of British Columbia–UTokyo Centre for Quantum Materials, and the Canada First Research Excellence Fund, Quantum Materials and Future Technologies Program. This project is also funded by the Natural Sciences and Engineering Research Council of Canada (NSERC), the Canada Foundation for Innovation (CFI); the British Columbia Knowledge Development Fund; the Department of National Defence; the Mitacs Accelerate Program; and the QuantEmX Program of the Institute for Complex Adaptive Matter; the Canada Research Chair Program (A.D.), and the Canadian Institute for Advanced Research Quantum Materials Program (A.D.). Use of the CLS (QMSC), a national research facility of the University of Saskatchewan, is supported by CFI, NSERC, the National Research Council, the Canadian Institutes of Health Research, the Government of Saskatchewan, and the University of Saskatchewan. The DMFT work was funded in part by the Deutsche Forschungsgemeinschaft (DFG, German Research Foundation) under Germany's Excellence Strategy–EXC-2111–390814868. M.V., M.C., and G.S., acknowledge support from the DFG (German Science Foundation) through FOR 5249 QUAST (Project-ID 449872909), EXC2147 ct.qmat (Project-ID 390858490), and SFB 1170 ToCoTronics (Project-ID 258499086), respectively. P.C.M. acknowledges the support from NSERC; S.S. acknowledges support by the Netherlands Organisation for Scientific Research (NWO 019.223EN.014, Rubicon 2022-3). F.B.K. acknowledges funding from the Ministerium für Kultur und Wissenschaft des Landes Nordrhein-Westfalen (NRW-Rückkehrprogramm). The Flatiron Institute is a division of the Simons Foundation.

Author affiliations: [a]Department of Physics, Massachusetts Institute of Technology, Cambridge, MA 02139; [b]Center for Computational Quantum Physics, Flatiron Institute, New York, NY 10010; [c]Department of Physics and Astronomy, University of British Columbia, Vancouver, BC V6T 1Z1, Canada; [d]Quantum Matter Institute, University of British Columbia, Vancouver, BC V6T 1Z4, Canada; [e]Canadian Light Source, Inc., 44 Innovation Boulevard, Saskatoon, SK S7N 2V3, Canada; [f]Max IV Laboratory, Lund University, Lund 22100, Sweden; [g]National Synchrotron Light Source II, Brookhaven National Laboratory, Upton, NY 11973; [h]Advanced Light Source, Lawrence Berkeley National Laboratory, Berkeley, CA 94720; [i]Max Planck Institute for Solid State Research, Stuttgart 70569, Germany; [j]Institut für Theoretische Physik und Astrophysik and Würzburg-Dresden Cluster of Excellence ct.qmat, Universität Würzburg, Würzburg 97074, Germany; [k]Department of Physics and Arnold Sommerfeld Center for Theoretical Physics, Ludwig-Maximilians-Universität München, Munich D-80333, Germany; [l]Munich Center for Quantum Science and Technology, München D-80799, Germany; [m]Institute for Theoretical Physics, University of Cologne, Cologne 50937, Germany; [n]Université Paris-Saclay, CNRS, Commissariat à l'Énergie Atomique et aux Énergies Alternatives, Institut de Physique Théorique, Gif-sur-Yvette 91191, France; [o]Department of Physics, University of Tokyo, Tokyo 113-0033, Japan; [p]Institute for Functional Matter and Quantum Technologies, University of Stuttgart, Stuttgart 70569, Germany; [q]Collège de France, 11 Place Marcelin Berthelot, Paris 75005, France; [r]Centre de Physique Théorique, CNRS, Ecole Polytechnique, Palaiseau F-91128, France; and [s]Department of Quantum Matter Physics, Université de Genève, Genève CH-1211, Switzerland

1. C. Kittel, *Introduction to Solid State Physics* (Wiley, ed. 8, 2005).
2. D. L. Bergman, C. Wu, L. Balents, Band touching from real-space topology in frustrated hopping models. *Phys. Rev. B* **78**, 125104 (2008).
3. M. Kang *et al.*, Dirac fermions and flat bands in the ideal kagome metal FeSn. *Nat. Mater.* **19**, 163–169 (2020).
4. M. Kang *et al.*, Topological flat bands in frustrated kagome lattice CoSn. *Nat. Commun.* **11**, 4004 (2020).
5. A. C. Jacko, J. O. Fjærestad, B. J. Powell, A unified explanation of the Kadowaki-Woods ratio in strongly correlated metals. *Nat. Phys.* **5**, 422–425 (2009).
6. G. R. Stewart, Heavy-fermion systems. *Rev. Mod. Phys.* **56**, 755–787 (1984).
7. M. Imada, A. Fujimori, Y. Tokura, Metal-insulator transitions. *Rev. Mod. Phys.* **70**, 1039–1263 (1998).
8. A. Georges, L. D. Medici, J. Mravlje, Strong correlations from Hund's coupling. *Annu. Rev. Condens. Matter Phys.* **4**, 137–178 (2013).
9. A. Georges, G. Kotliar, The Hund-metal path to strong electronic correlations. *Phys. Today* **77**, 46–53 (2024).
10. B. J. Ramshaw *et al.*, Quasiparticle mass enhancement approaching optimal doping in a high-T_c superconductor. *Science* **348**, 317–320 (2015).
11. B. Michon *et al.*, Thermodynamic signatures of quantum criticality in cuprate superconductors. *Nature* **567**, 218–222 (2019).
12. Z. P. Yin, K. Haule, G. Kotliar, Kinetic frustration and the nature of the magnetic and paramagnetic states in iron pnictides and iron chalcogenides. *Nat. Mater.* **10**, 932–935 (2011).
13. H. Li *et al.*, Fermiology and electron dynamics of trilayer nickelate $La_4Ni_3O_{10}$. *Nat. Commun.* **8**, 704 (2017).
14. J. Yang *et al.*, Orbital-dependent electron correlation in double-layer nickelate $La_3Ni_2O_7$. *Nat. Commun.* **15**, 4373 (2024).
15. Y. Cao, Y. Yang, Flat bands promoted by Hund's rule coupling in the candidate double-layer high-temperature superconductor $La_3Ni_2O_7$. *Phys. Rev. B* **109**, L081105 (2024).
16. J. Mravlje *et al.*, Coherence-incoherence crossover and the mass-renormalization puzzles in Sr_2RuO_4. *Phys. Rev. Lett.* **106**, 096401 (2011).
17. T. Kondo *et al.*, Orbital-dependent band narrowing revealed in an extremely correlated Hund's metal emerging on the topmost layer of Sr_2RuO_4. *Phys. Rev. Lett.* **117**, 247001 (2016).
18. L. Balents, C. R. Dean, D. K. Efetov, A. F. Young, Superconductivity and strong correlations in moiré flat bands. *Nat. Phys.* **16**, 725–733 (2020).
19. M. Serlin *et al.*, Intrinsic quantized anomalous Hall effect in a moiré heterostructure. *Science* **367**, 900–903 (2020).
20. H. Park *et al.*, Observation of fractionally quantized anomalous Hall effect. *Nature* **622**, 74–79 (2023).
21. J.-W. Rhim, K. Kim, B.-J. Yang, Quantum distance and anomalous Landau levels of flat bands. *Nature* **584**, 59–63 (2020).
22. T. Mizoguchi, M. Udagawa, Flat-band engineering in tight-binding models: Beyond the nearest-neighbor hopping. *Phys. Rev. B* **99**, 235118 (2019).
23. N. Regnault *et al.*, Catalogue of flat-band stoichiometric materials. *Nature* **603**, 824–828 (2022).
24. J. P. Wakefield *et al.*, Three-dimensional flat bands in pyrochlore metal $CaNi_2$. *Nature* **623**, 301–306 (2023).
25. P. M. Neves *et al.*, Crystal net catalog of model flat band materials. *NPJ Comput. Mater.* **10**, 39 (2024).
26. J. G. Checkelsky, B. A. Bernevig, P. Coleman, Q. Si, S. Paschen, Flat bands, strange metals and the Kondo effect. *Nat. Rev. Mater.* **9**, 509–526 (2024), 10.1038/s41578-023-00644-z.
27. F. Baboux *et al.*, Bosonic condensation and disorder-induced localization in a flat band. *Phys. Rev. Lett.* **116**, 066402 (2016).
28. D. Leykam, A. Andreanov, S. Flach, Artificial flat band systems: From lattice models to experiments. *Adv. Phys.: X* **3**, 1473052 (2018).
29. T.-X. Ma, Q.-S. Fan, C. Zhang, Y.-S. Wang, Acoustic flatbands in phononic crystal defect lattices. *J. Appl. Phys.* **129**, 145104 (2021).
30. S. Tacchi *et al.*, Experimental observation of flat bands in one-dimensional chiral magnonic crystals. *Nano Lett.* **23**, 6776–6783 (2023).
31. M. Pan *et al.*, Growth of mesoscale ordered two-dimensional hydrogen-bond organic framework with the observation of flat band. *Phys. Rev. Lett.* **130**, 036203 (2023).
32. S. Kondo *et al.*, LiV_2O_4: A heavy fermion transition metal oxide. *Phys. Rev. Lett.* **78**, 3729 (1997).
33. C. Urano *et al.*, LiV_2O_4 spinel as a heavy-mass Fermi liquid: Anomalous transport and role of geometrical frustration. *Phys. Rev. Lett.* **85**, 1052–1055 (2000).
34. U. Niemann *et al.*, Crystallization of heavy fermions via epitaxial strain in spinel LiV_2O_4 thin film. *Proc. Natl. Acad. Sci. U.S.A.* **120**, e2215722120 (2023).
35. S.-H. Lee, Y. Qiu, C. Broholm, Y. Ueda, J. J. Rush, Spin fluctuations in a magnetically frustrated metal LiV_2O_4. *Phys. Rev. Lett.* **86**, 5554–5557 (2001).
36. S. Burdin, D. R. Grempel, A. Georges, Heavy-fermion and spin-liquid behavior in a kondo lattice with magnetic frustration. *Phys. Rev. B* **66**, 045111 (2002).
37. J. Hopkinson, P. Coleman, LiV_2O_4: Frustration induced heavy fermion metal. *Phys. Rev. Lett.* **89**, 267201 (2002).
38. Y. Yamashita, K. Ueda, Spin-orbital fluctuations and a large mass enhancement in LiV_2O_4. *Phys. Rev. B* **67**, 195107 (2003).
39. P. E. Jönsson *et al.*, Correlation-driven heavy-fermion formation in LiV_2O_4. *Phys. Rev. Lett.* **99**, 167402 (2007).
40. Y. Shimizu *et al.*, An orbital-selective spin liquid in a frustrated heavy fermion spinel LiV_2O_4. *Nat. Commun.* **3**, 981 (2012).
41. V. I. Anisimov *et al.*, Electronic structure of the heavy fermion metal LiV_2O_4. *Phys. Rev. Lett.* **83**, 364–367 (1999).
42. H. Kusunose, S. Yotsuhashi, K. Miyake, Formation of a heavy quasiparticle state in the two-band Hubbard model. *Phys. Rev. B* **62**, 4403–4407 (2000).
43. I. A. Nekrasov *et al.*, Orbital state and magnetic properties of LiV_2O_4. *Phys. Rev. B* **67**, 085111 (2003).
44. R. Arita, K. Held, A. V. Lukoyanov, V. I. Anisimov, Doped mott insulator as the origin of heavy-fermion behavior in LiV_2O_4. *Phys. Rev. Lett.* **98**, 166402 (2007).
45. H. Takagi *et al.*, Transport properties of metallic LiV_2O_4 single crystals–Heavy mass Fermi liquid behavior. *Mater. Sci. Eng. B* **63**, 147–150 (1999).
46. T. Senthil, S. Sachdev, M. Vojta, Fractionalized fermi liquids. *Phys. Rev. Lett.* **90**, 216403 (2003).
47. S. Sachdev, Holographic metals and the fractionalized Fermi liquid. *Phys. Rev. Lett.* **105**, 151602 (2010).
48. X. Deng *et al.*, How bad metals turn good: Spectroscopic signatures of resilient quasiparticles. *Phys. Rev. Lett.* **110**, 086401 (2013).
49. A. Georges, G. Kotliar, W. Krauth, M. J. Rozenberg, Dynamical mean-field theory of strongly correlated fermion systems and the limit of infinite dimensions. *Rev. Mod. Phys.* **68**, 13–125 (1996).
50. M. Grundner *et al.*, LiV_2O_4: Hund-assisted orbital-selective mottness. *Phys. Rev. B* **112**, L041106 (2025).
51. J. Huang *et al.*, Non-Fermi liquid behaviour in a correlated flat-band pyrochlore lattice. *Nat. Phys.* **20**, 603–609 (2024).
52. A. Shimoyamada *et al.*, Heavy-fermion-like state in a transition metal oxide LiV_2O_4 single crystal: Indication of Kondo resonance in the photoemission spectrum. *Phys. Rev. Lett.* **96**, 026403 (2006).
53. S. Backes, Y. Nomura, R. Arita, H. Shinaoka, Ab initio study on heavy-fermion behavior in LiV_2O_4: Role of Hund's coupling and stability. *Phys. Rev. B* **111**, L041102 (2025).

54. L. De' Medici, S. R. Hassan, M. Capone, X. Dai, Orbital-selective Mott transition out of band degeneracy lifting. *Phys. Rev. Lett.* **102**, 126401 (2009).
55. F. B. Kugler, G. Kotliar, Is the orbital-selective Mott phase stable against interorbital hopping? *Phys. Rev. Lett.* **129**, 096403 (2022).
56. M. Crispino *et al.*, Paradigm for finding d-electron heavy fermions: The case of Cr-doped CsFe2As2. arXiv [Preprint] (2023). http://arxiv.org/abs/2312.06511 (Accessed 17 July 2024).
57. X. Deng *et al.*, Signatures of Mottness and Hundness in archetypal correlated metals. *Nat. Commun.* **10**, 2721 (2019).
58. K. M. Stadler, G. Kotliar, A. Weichselbaum, J. Von Delft, Hundness versus mottness in a three-band Hubbard-Hund model: On the origin of strong correlations in Hund metals. *Ann. Phys.* **405**, 365–409 (2019).
59. P. Werner, E. Gull, M. Troyer, A. J. Millis, Spin freezing transition and non-Fermi-liquid self-energy in a three-orbital model. *Phys. Rev. Lett.* **101**, 166405 (2008).
60. S. Samanta *et al.*, Emergence of flat bands and ferromagnetic fluctuations via orbital-selective electron correlations in Mn-based kagome metal. *Nat. Commun.* **15**, 5376 (2024).
61. A. Kowalski, A. Hausoel, M. Wallerberger, P. Gunacker, G. Sangiovanni, State and superstate sampling in hybridization-expansion continuous-time quantum Monte Carlo. *Phys. Rev. B* **99**, 155112 (2019).
62. S. Nakatsuji *et al.*, Heavy-mass Fermi liquid near a ferromagnetic instability in layered Ruthenates. *Phys. Rev. Lett.* **90**, 137202 (2003).
63. Y. Okamoto, T. Shimizu, J. Yamaura, Y. Kiuchi, Z. Hiroi, Itinerant-electron magnet of the pyrochlore lattice: Indium-doped YMn2Zn20. *J. Phys. Soc. Jpn.* **79**, 093712 (2010).
64. H. Wada *et al.*, Spin fluctuations of $Y(Mn_{1-x}Al_x)_2$ and $Y_{1-x}Sc_xMn_2$. *J. Magn. Magn. Mater.* **70**, 17–19 (1987).
65. Y. Zhang *et al.*, Emergence of Kondo lattice behavior in a van der Waals itinerant ferromagnet, Fe_3GeTe_2. *Sci. Adv.* **4**, eaao6791 (2018).
66. Y. Kim *et al.*, Kondo interaction in FeTe and its potential role in the magnetic order. *Nat. Commun.* **14**, 4145 (2023).
67. H. Mamiya, M. Onoda, Electronic states of vanadium spinels MgV_2O_4 and ZnV_2O_4. *Solid State Commun.* **95**, 217–221 (1995).
68. G. M. Kalvius *et al.*, Magnetic properties of geometrically frustrated $Zn_xLi_{1x}V_2O_4$. *Phys. B: Condens. Matter* **326**, 470–474 (2003).
69. A. Manthiram, J. B. Goodenough, Refinement of the critical V-V separation for spontaneous magnetism in oxides. *Can. J. Phys.* **65**, 1309–1317 (1987).
70. T. Yajima *et al.*, Heavy-fermion metallic state and Mott transition induced by Li-ion intercalation in LiV_2O_4 epitaxial films. *Phys. Rev. B* **104**, 245104 (2021).
71. Y. Wang, Heavy-fermions in frustrated Hund's metal with portions of incipient flat-bands. arXiv [Preprint] (2024). http://arxiv.org/abs/2401.16770 (Accessed 2 May 2024).
72. S. Peng *et al.*, Flat bands and distinct density wave orders in correlated Kagome superconductor $CsCr_3Sb_5$. arXiv [Preprint] (2024). https://arxiv.org/abs/2406.17769v2 (Accessed 2 October 2024).
73. E. Walter *et al.*, Uncovering non-Fermi-liquid behavior in Hund metals: Conformal field theory analysis of an SU(2) × SU(3) spin-orbital Kondo model. *Phys. Rev. X* **10**, 031052 (2020).
74. Y. Wang *et al.*, Global phase diagram of a spin-orbital Kondo impurity model and the suppression of Fermi-liquid scale. *Phys. Rev. Lett.* **124**, 136406 (2020).
75. F. B. Kugler, Orbital differentiation in Hund metals. *Phys. Rev. B* **100**, 115159 (2019).
76. K. M. Stadler, G. Kotliar, S.-S. B. Lee, A. Weichselbaum, J. Von Delft, Differentiating Hund from Mott physics in a three-band Hubbard-Hund model: Temperature dependence of spectral, transport, and thermodynamic properties. *Phys. Rev. B* **104**, 115107 (2021).
77. S. Das *et al.*, Crystallography, magnetic susceptibility, heat capacity, and electrical resistivity of heavy-fermion LiV_2O_4 single crystals grown using a self-flux technique. *Phys. Rev. B* **76**, 054418 (2007).
78. D. R. Hamann, Optimized norm-conserving Vanderbilt pseudopotentials. *Phys. Rev. B* **88**, 085117 (2013).
79. M. J. van Setten *et al.*, The PseudoDojo: Training and grading a 85 element optimized norm-conserving pseudopotential table. *Comput. Phys. Commun.* **226**, 39–54 (2018).
80. A. A. Mostofi *et al.*, An updated version of wannier90: A tool for obtaining maximally-localised Wannier functions. *Comput. Phys. Commun.* **185**, 2309–2310 (2014).
81. F. Aryasetiawan *et al.*, Frequency-dependent local interactions and low-energy effective models from electronic structure calculations. *Phys. Rev. B* **70**, 195104 (2004).
82. K. Nakamura *et al.*, RESPACK: An ab initio tool for derivation of effective low-energy model of material. *Comput. Phys. Commun.* **261**, 107781 (2021).
83. O. Parcollet *et al.*, TRIQS: A toolbox for research on interacting quantum systems. *Comput. Phys. Commun.* **196**, 398–415 (2015).
84. P. Seth, I. Krivenko, M. Ferrero, O. Parcollet, TRIQS/CTHYB: A continuous-time quantum Monte Carlo hybridisation expansion solver for quantum impurity problems. *Comput. Phys. Commun.* **200**, 274–284 (2016).
85. M. Aichhorn *et al.*, TRIQS/DFTTools: A TRIQS application for *ab initio* calculations of correlated materials. *Comput. Phys. Commun.* **204**, 200–208 (2016).
86. M. E. Merkel, A. Carta, S. Beck, A. Hampel, Solid_dmft: Gray-boxing DFT+DMFT materials simulations with TRIQS. *J. Open Source Softw.* **7**, 4623 (2022).
87. H. LaBollita, J. Kaye, A. Hampel, Stabilizing the calculation of the self-energy in dynamical mean-field theory using constrained residual minimization. *Phys. Rev. B* 111, 115155 (2025).
88. F. A. Wolf, A. Go, I. P. McCulloch, A. J. Millis, U. Schollwöck, Imaginary-time matrix product state impurity solver for dynamical mean-field theory. *Phys. Rev. X* **5**, 041032 (2015).
89. N.-O. Linden, M. Zingl, C. Hubig, O. Parcollet, U. Schollwöck, Imaginary-time matrix product state impurity solver in a real material calculation: Spin-orbit coupling in Sr_2RuO_4. *Phys. Rev. B* **101**, 041101 (2020).
90. J. Karp *et al.*, Sr_2MoO_4 and Sr_2RuO_4: Disentangling the roles of Hund's and van Hove Physics. *Phys. Rev. Lett.* **125**, 166401 (2020).
91. F. Verstraete, J. J. García-Ripoll, J. I. Cirac, Matrix product density operators: Simulation of finite-temperature and dissipative systems. *Phys. Rev. Lett.* **93**, 207204 (2004).
92. U. Schollwöck, The density-matrix renormalization group in the age of matrix product states. *Ann. Phys.* **326**, 96–192 (2011).
93. F. B. Kugler *et al.*, Strongly correlated materials from a numerical renormalization group perspective: How the Fermi-liquid state of Sr_2RuO_4 emerges. *Phys. Rev. Lett.* **124**, 016401 (2020).
94. F. B. Kugler, C.-J. Kang, G. Kotliar, Low-energy perspective on two-orbital Hund metals and the case of $LaNiO_2$. *Phys. Rev. B* **110**, 155101 (2024).
95. D. Oh *et al.*, Hund flat band in a frustrated spinel oxide. Harvard Dataverse. https://doi.org/10.7910/DVN/IOGG6F. Deposited 23 June 2025.
96. C. Hubig *et al.*, The SyTen Toolkit. SyTen. http://syten.eu. Accessed 1 May 2023.